

Wide-Bandgap Organic Crystals: Enhanced Optical-to-Terahertz Nonlinear Frequency Conversion at Near-Infrared Pumping

Deokjoong Kim, Won Tae Kim, Jae-Hyun Han, Ji-Ah Lee, Seung-Heon Lee, Bong Joo Kang, Mojca Jazbinsek, Woojin Yoon, Hoseop Yun, Dongwook Kim, Stein van Bezouw, Jochen Campo, Wim Wenseleers, Fabian Rotermund,* and O-Pil Kwon*

Enhanced terahertz (THz) wave generation is demonstrated in nonlinear organic crystals through refractive index engineering, which improves phase matching characteristics substantially. Unlike conventional low-bandgap nonlinear organic crystals, the newly designed benzimidazolium-based HMI (2-(4-hydroxy-3-methoxystyryl)-1,3-dimethyl-1H-benzimidazol-3-ium) chromophore possesses a relatively wide bandgap. This reduces the optical group index in the near-infrared, allowing better phase matching with the generated THz waves, and leads to high optical-to-THz conversion. A unique feature of the HMI-based crystals, compared to conventional wide-bandgap aniline-based crystals, is their remarkably larger macroscopic optical nonlinearity, a one order of magnitude higher diagonal component in macroscopic nonlinear susceptibility than NPP ((1-(4-nitrophenyl)pyrrolidin-2-yl)methanol) crystals. The HMI-based crystals also exhibit much higher thermal stability, with a melting temperature T_m above 250 °C, versus aniline-based crystals (116 °C for NPP). With pumping at the technologically important wavelength of 800 nm, the proposed HMI-based crystals boost high optical-to-THz conversion efficiency, comparable to benchmark low-bandgap quinolinium crystals with state-of-the-art macroscopic nonlinearity. This performance is due to the excellent phase matching enabled by decreasing optical group indices in the near-infrared through wide-bandgap chromophores. The proposed wide-bandgap design is a promising way to control the refractive index of various nonlinear organic materials for enhanced frequency conversion processes.


1. Introduction

Research interest in broadband coherent sources in the terahertz (THz) frequency range is growing rapidly due to advanced applications in THz spectroscopy and imaging, as well as fundamental studies of the ultrafast dynamics of diverse materials, and nonlinear THz photonics.^[1–5] To date, designing and developing highly efficient THz wave generators remains challenging.^[4,6–10] Nonlinear optical organic crystals which exploit either optical rectification (OR) or difference frequency generation (DFG) processes have been reported to provide excellent optical-to-THz conversion.^[7,11–18] For example, benchmark nonlinear organic crystals with state-of-the-art macroscopic optical nonlinearity have demonstrated high THz wave generation efficiencies of up to a few percent when pumped by infrared (IR) pulses in the wavelength range of 1200–1600 nm.^[13–17] An alternative to employing pump sources in this range is to pump at a near-IR wavelength near 800 nm. This is a very important practical wavelength and is available with widespread femtosecond Ti:sapphire

D. Kim, J.-H. Han, J.-A. Lee, Dr. S.-H. Lee, Prof. O-P. Kwon
Department of Molecular Science and Technology
Ajou University
Suwon 443-749, Korea
E-mail: opilkwon@ajou.ac.kr

W. T. Kim, Dr. B. J. Kang, Prof. F. Rotermund
Department of Physics
Korea Advanced Institute of Science and Technology (KAIST)
Daejeon 34141, Korea
E-mail: rotermund@kaist.ac.kr

Dr. M. Jazbinsek
Institute of Computational Physics
Zurich University of Applied Sciences (ZHAW)
Winterthur 8401, Switzerland

 The ORCID identification number(s) for the author(s) of this article can be found under <https://doi.org/10.1002/adom.201902099>.

W. Yoon, Prof. H. Yun
Department of Chemistry and Department of Energy Systems Research
Ajou University
Suwon 443-749, Korea

Prof. D. Kim
Department of Chemistry
Kyonggi University
San 94-6, Iui-dong, Yeongtong-gu, Suwon-si, Gyeonggi 443-760, Korea
S. van Bezouw, Dr. J. Campo, Prof. W. Wenseleers
Department of Physics
University of Antwerp
Campus Drie Eiken (CDE)
Universiteitsplein 1, Wilrijk B-2610, Belgium

DOI: 10.1002/adom.201902099

laser technologies. However, the approach has resulted in relatively low THz wave generation efficiency with limited spectral bandwidth. The poor performance is basically due to poor phase matching between the optical pump and the generated THz waves in most nonlinear organic crystals at this wavelength.

The THz wave generation efficiency of nonlinear organic crystals is mainly affected by two material-specific parameters, namely the macroscopic second order nonlinear optical susceptibility and the phase matching condition.^[12,15,19] To improve optical-to-THz conversion efficiency, most recent studies have focused on enhancing the macroscopic second-order optical nonlinearity of the organic crystals. Following this concept, the so-called “low-bandgap approach”—introducing highly nonlinear optical low-bandgap chromophores into crystals—has been widely investigated.^[7a,b,17,20–23]

In general, decreasing the bandgap between the highest occupied molecular orbital (HOMO) and the lowest unoccupied molecular orbital (LUMO) in a chromophore increases its molecular optical nonlinearity.^[24] A lower bandgap means a longer wavelength of absorption maximum λ_{max} (e.g., λ_{max} of low-bandgap chromophores ≥ 430 nm in solution). In nonlinear optics this is commonly known as the nonlinearity/transparency tradeoff.^[24] In addition, since the causality fundamentally links the refractive index dispersion $n(\lambda)$ of the optical materials to the absorption coefficient $\alpha(\lambda)$ through the Kramers–Kronig relation,^[25] having a lower bandgap in the organic crystals results in increasing the refractive index for optical wavelengths in the near-IR.

For efficient THz wave generation, the difference $\Delta n = n_{\text{g,opt}} - n_{\text{THz}}$ between the optical group index $n_{\text{g,opt}}$ and the THz (phase) index n_{THz} should be as small as possible, ensuring good phase matching.^[12,15,19] In most benchmark nonlinear organic crystals, the phase matching condition for THz wave generation is only well satisfied when the optical pump is in the IR range of 1200–1600 nm, but particularly not below 1000 nm, where the refractive index already increases due to small HOMO-LUMO gaps.^[15,16,26] Therefore, reducing the refractive index of organic crystals at near-IR optical pump wavelengths, which approaches the refractive index in the THz region, is beneficial to achieving high THz wave generation efficiency, even near the technologically important wavelength of 800 nm, due to better phase matching.

In this work, instead of following the low-bandgap approach employed for the majority of benchmark nonlinear organic crystals, we demonstrate the potential of refractive-index engineering employing the so-called “wide-bandgap approach,” introducing wide-bandgap chromophores into crystals instead of low-bandgap chromophores (see **Figure 1a**). By introducing chromophores with a wider HOMO-LUMO bandgap, the wavelength of absorption maximum λ_{max} decreases (see the horizontal arrow in **Figure 1a**). A blue-shifted absorption is accompanied by decreased phase and group refractive indices (n_{opt} and $n_{\text{g,opt}}$ respectively) in the near-IR region, as illustrated by the vertical arrow in **Figure 1a**), which is required to improve the phase matching condition for efficient THz wave generation. The newly designed stilbene-type benzimidazolium-based chromophores exhibit a large bandgap (e.g., 364 nm of the wavelength of absorption maximum λ_{max} in methanol, which is close to the shortest absorption wavelength achievable in

organic push-pull aromatic compounds), while still maintaining a remarkably large nonlinear optical response (first hyperpolarizability β). The benzimidazolium-based crystals are found to provide a large optical-to-THz conversion efficiency for the near-IR pump wavelength of 800 nm due to better phase matching with a lower refractive index, comparable to benchmark low-bandgap organic crystals with state-of-the-art macroscopic optical nonlinearity.

2. Results and Discussions

2.1. Design of Wide-Bandgap Chromophores

Figure 1b shows the chemical structure of the newly designed wide-bandgap stilbene-type cationic chromophore HMI (2-(4-hydroxy-3-methoxystyryl)-1,3-dimethyl-1H-benzimidazol-3-ium). For the refractive-index engineering based on wide-bandgap approach, we propose modifying a benchmark organic nonlinear crystal (which we call the mother crystal here) with a perfectly parallel alignment of low-bandgap nonlinear optical chromophores so that the overall molecular ordering features in the new wide-bandgap crystal are maintained. In many cases, modifying a part of the chemical structure of the mother crystals results in a large change in the overall molecular ordering features, leading to a large change of refractive index in an unpredictable direction. The main goal of the newly designed wide-bandgap crystals is to maintain the overall molecular ordering features of the mother crystals, and keep the other desired physical properties (e.g., perfectly parallel alignment of nonlinear optical chromophores for maximizing the macroscopic optical nonlinearity) while only modifying the dispersion characteristics (i.e., changing and optimizing the phase matching conditions for THz wave generation).

In this work, we chose the benchmark low-bandgap nonlinear organic crystals HMQ-TMS (2-(4-hydroxy-3-methoxystyryl)-1-methylquinolinium 2,4,6-trimethylbenzenesulfonate, see **Figure 1c**) as the mother crystal. HMQ-TMS exhibits high THz wave generation efficiency due to a large macroscopic optical nonlinearity.^[16,20] For THz wave generation, HMQ-TMS crystals based on the low-bandgap cationic chromophore HMQ (2-(4-hydroxy-3-methoxystyryl)-1-methylquinolinium) are much better phase-matchable at IR pump wavelengths between 1100 and 1500 nm) than near 800 nm, as mentioned above. To keep the overall molecular ordering features of the low-bandgap mother crystal, the newly designed wide-bandgap crystals need to provide very similar intermolecular interactions (in this work, including interionic interactions) and similar space filling characteristics (i.e., maintaining the van der Waals volume of the constituting cations and anions).^[17b,23a]

In mother HMQ-TMS crystals, the HMQ cationic chromophore consists of a 4-hydroxy-3-methoxy phenyl electron donor group and a 1-methylquinolinium electron acceptor group (see **Figure 1c**). To maintain the overall molecular ordering features of the HMQ-TMS crystals, but modify the refractive index characteristics through a wider HOMO-LUMO gap, the newly designed wide-bandgap HMI cationic chromophore consists of identical electron donor groups, but different electron acceptor groups. We chose the benzimidazolium group

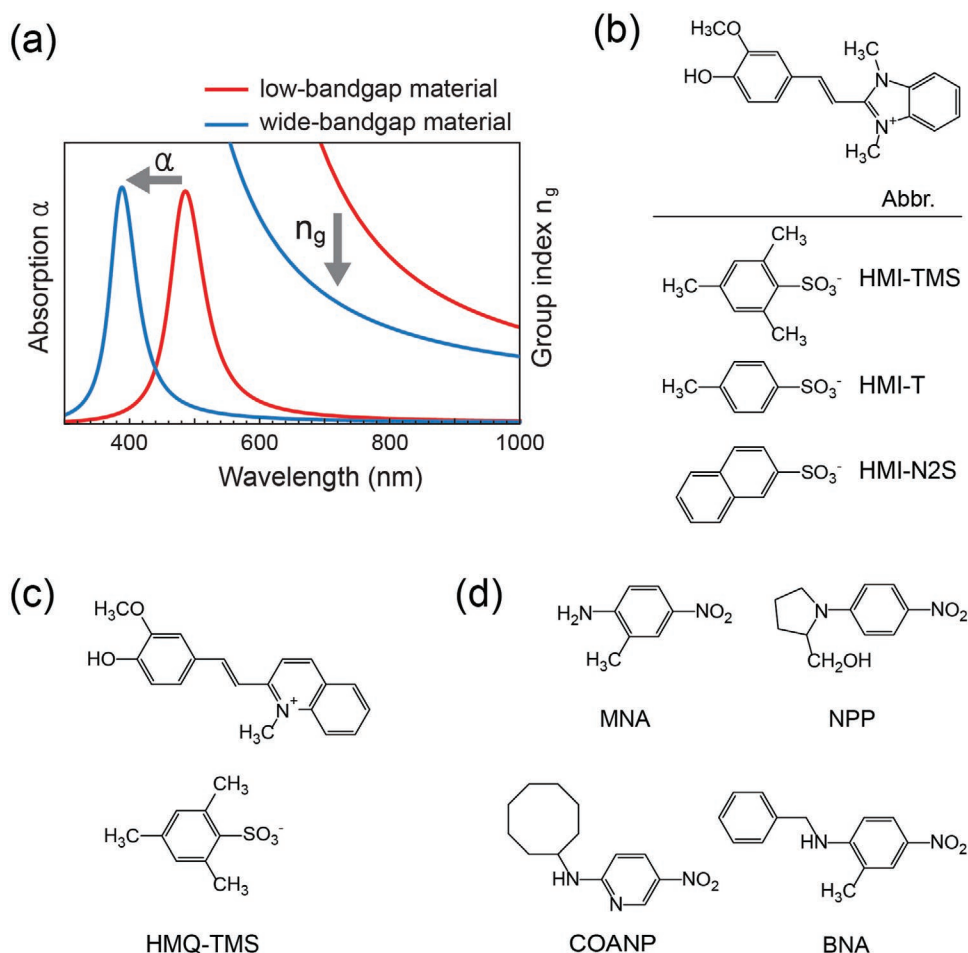


Figure 1. a) Schematic illustration of the wide-bandgap approach for organic materials for application as efficient THz generators. Introducing wide-bandgap chromophores with a blue-shifted absorption band effectively reduces the group index in the near-IR. The curves are from a single-oscillator Lorentz model (see, e.g., ref. [26a]) with different resonant wavelengths: 500 nm (red) and 400 nm (blue). The chemical structures of the nonlinear optical b) wide-bandgap stilbene-type HMI-based crystals introduced in this work, while the c) low-bandgap stilbene-type HMQ-TMS crystals, and d) wide-bandgap aniline-type crystals were taken from the literature.

(1,3-dimethyl-1H-benzimidazol-3-ium) which is a relatively weak electron acceptor compared to the quinolinium groups used in benchmark low-bandgap nonlinear optical crystals including HMQ-TMS crystals.^[27,28] Since the van der Waals volume and most of the chemical structure of the HMI chromophore is very similar to the mother HMQ chromophore, the HMI-based crystals may exhibit similar overall molecular ordering features and corresponding physical properties, even though the refractive index decreases. As a result, introducing the HMI cation keeps the overall characteristics of the long-wavelength refractive index of the benchmark HMQ-TMS crystals unimpaired (including the overall characteristics for THz wave generation), but the refractive index in the near-IR region is expected to decrease due to the wide bandgap of the HMI cation, as illustrated in Figure 1a.

The wide-bandgap HMI cationic chromophore possesses a stilbene-type structure with two aromatic rings in the π -conjugated bridge (benzimidazolium and phenolic rings) like the benchmark highly nonlinear organic ionic crystals (e.g., the selected mother HMQ-TMS crystals as mentioned above)

which possess high thermal stability.^[7a,17,20,30] Accordingly, the HMI cationic chromophore-based crystals are expected to exhibit a high thermal stability, as was also confirmed experimentally (see Section 2.3). Note that previously reported wide-bandgap crystals are based on aniline-type chromophores having only one aromatic ring in the π -conjugated bridge, as shown in Figure 1d. The aniline-type wide-bandgap crystals have been shown to possess a relatively low macroscopic optical nonlinearity and low thermal stability, which may limit practical applications.^[24,29]

To achieve a (perfectly) parallel alignment of the nonlinear optical HMI cationic chromophores to maximize macroscopic second-order optical nonlinearity in the crystalline state, it is necessary to adjust the space filling characteristics of the counter anions. Here we chose three benzenesulfonate anions, TMS (2,4,6-trimethylbenzenesulfonate), T (4-methylbenzenesulfonate) and N2S (naphthalene-2-sulfonate) incorporated in the HMI-TMS, HMI-T and HMI-N2S crystals, respectively. To investigate their physical and (nonlinear) optical properties, X-ray single crystal structure analyses of all three HMI-based

Table 1. Summary of the physical properties and crystal systems of the wide-bandgap stilbene-type HMI-TMS crystal introduced in this work, compared with previously developed aniline-type crystals.

	HMI-TMS	MNA	NPP	COANP	BNA
λ_{\max} (nm) in solution	364 methanol	374 methanol	390 ethano [^{29a}]	361 dioxane [²⁴]	383 ethano [^{29c}]
T_m (°C)	259	135	116 [^{29a}]	71 [^{29b}]	105 [^{29c}]
Crystal system	monoclinic <i>Pn</i>	monoclinic <i>Ia</i> [^{29d}]	monoclinic <i>P2</i> [^{29e}]	orthorhombic <i>Pca2</i> [^{29f}]	orthorhombic <i>Pna2</i> [^{29g}]
β_{\max} (EXP) (10^{-30} esu)	77.4	16.2	28.8	24.1	21.9
θ_p (degree)	3.0	18.3	56.9	57.7	32.5
order parameter $\cos^3\theta_p$	1.0	0.86	0.16	0.15	0.6
number density N ($10^{27}/\text{m}^3$)	1.61	5.51	3.83	3.06	3.14
largest diagonal β_{iii}^{eff} (10^{-30} esu)	$\beta_{111}^{\text{eff}} = 77.1$	$\beta_{111}^{\text{eff}} = 13.5$	$\beta_{222}^{\text{eff}} = 2.9$	$\beta_{333}^{\text{eff}} = 3.2$	$\beta_{333}^{\text{eff}} = 12.3$
largest diagonal $N\beta_{iii}^{\text{eff}}$ (10^{-3} esu m^{-3})	$N\beta_{111}^{\text{eff}} = 124$	$N\beta_{111}^{\text{eff}} = 74.5$	$N\beta_{222}^{\text{eff}} = 11.2$	$N\beta_{333}^{\text{eff}} = 9.8$	$N\beta_{333}^{\text{eff}} = 38.5$
largest off-diagonal β_{ijk}^{eff} (10^{-30} esu)	$\beta_{221}^{\text{eff}} = 1.2$	$\beta_{223}^{\text{eff}} = 0.8$	$\beta_{332}^{\text{eff}} = 12.3$	$\beta_{223}^{\text{eff}} = 6.4$	$\beta_{223}^{\text{eff}} = 3.5$
largest off-diagonal $N\beta_{ijk}^{\text{eff}}$ (10^{-3} esu m^{-3})	$N\beta_{221}^{\text{eff}} = 1.9$	$N\beta_{223}^{\text{eff}} = 4.5$	$N\beta_{332}^{\text{eff}} = 46.9$	$N\beta_{223}^{\text{eff}} = 120$	$N\beta_{223}^{\text{eff}} = 11.1$
optical group index at 800 nm	2.14	–	–	1.69 [⁴⁷]	1.83 [⁴⁸]

crystals was performed (see the Experimental Section and Table 1).

Figure 2a shows the UV–vis absorption spectra of the HMI-based compounds. The wavelength of the absorption maximum λ_{\max} of the HMI cation in the HMI-based compounds is located in a very short region, about 364 nm in methanol, which is much shorter than in the benchmark nonlinear organic crystals; e.g., 439 nm for HMQ-TMS and 426 nm for OH1 (2-(3-(4-hydroxystyryl)-5,5-dimethylcyclohex-2-enylidene)malononitrile) crystals in methanol.^[20,31] It is even shorter (or similar) than those of aniline-type wide-bandgap crystals such as MNA (2-methyl-4-nitroaniline), NPP ((1-(4-nitrophenyl)pyrrolidin-2-yl) methanol), COANP (*N*-cyclooctyl-5-nitropyridin-2-amine) and BNA (*N*-benzyl-2-methyl-4-nitroaniline) as listed in Table 1.^[24,29]

It is worth noting that the wavelength of absorption maximum λ_{\max} of the HMI-based compounds (364 nm in methanol) is close to the shortest wavelength of the absorption maximum λ_{\max} (related to the HOMO-LUMO bandgap) reported for conventional push-pull aromatic compounds.^[24,29,32] Therefore, HMI-TMS crystals consisting of wide-bandgap HMI cations are expected to possess lower refractive indices at shorter wavelengths (e.g., the near-IR wavelength of 800 nm) than benchmark low-bandgap nonlinear optical organic crystals.

2.2. High Molecular Optical Nonlinearity

Interestingly, although HMI-based compounds exhibit an absorption band in the very short-wavelength region in the ultraviolet (UV), the microscopic optical nonlinearity of HMI cations is still very large, and particularly much larger than that

of aniline-type wide-bandgap chromophores. This has been demonstrated in both experimental and theoretical studies, as summarized below.

The molecular first hyperpolarizability (effective β_{zzz}), determined experimentally using Hyper-Rayleigh scattering (HRS) measurements on HMI-TMS in methanol at a wavelength of 1360 nm, is $\beta_{zzz,1360} = 68 \times 10^{-30}$ esu (see Figure 2b and Section A in the Supporting Information).^[33] Using accurate β dispersion models, as described in Section A in the Supporting Information, this value is extrapolated to yield the static first hyperpolarizability $\beta_{zzz,0} = 47 \times 10^{-30}$ esu. The estimated value of $\beta_{zzz,0}$ for HMI-TMS is much larger than that of *p*-nitroaniline with a comparable bandgap ($\lambda_{\max} = 347$ nm in chloroform) and $\beta_{zzz,0} = 17 \times 10^{-30}$ esu in chloroform, as determined using the same setup, and is in excellent agreement with the experimental results reported in the literature.^[34]

To gain better understanding of the correlation between the static hyperpolarizability and absorption characteristics of the benzimidazolium-based HMI-TMS chromophore, we also analyzed its lower-bandgap analogue, DAI-TMS ((2-(4-(dimethylamino)styryl)-1,3-dimethyl-1H-benzoimidazol-3-ium 2,4,6-trimethylbenzenesulfonate, see Figure S1 in the Supporting Information) consisting of the DAI (2-(4-(dimethylamino)styryl)-1,3-dimethyl-1H-benzoimidazol-3-ium) cation and TMS anion. The static hyperpolarizability $\beta_{zzz,0}$ is proportional to the third power of the absorption wavelength (λ_{\max}^3), the oscillator strength f_{osc} and the difference in dipole moment between the ground and excited state $\Delta\mu$.^[35] By comparing the contributions of HMI-TMS and DAI-TMS to $\beta_{zzz,0}$ (see details in Section A.2 in the Supporting Information), $\Delta\mu$ practically does not vary with different electron donor groups in the HMI and DAI cations, and the hyperpolarizability of HMI-TMS can

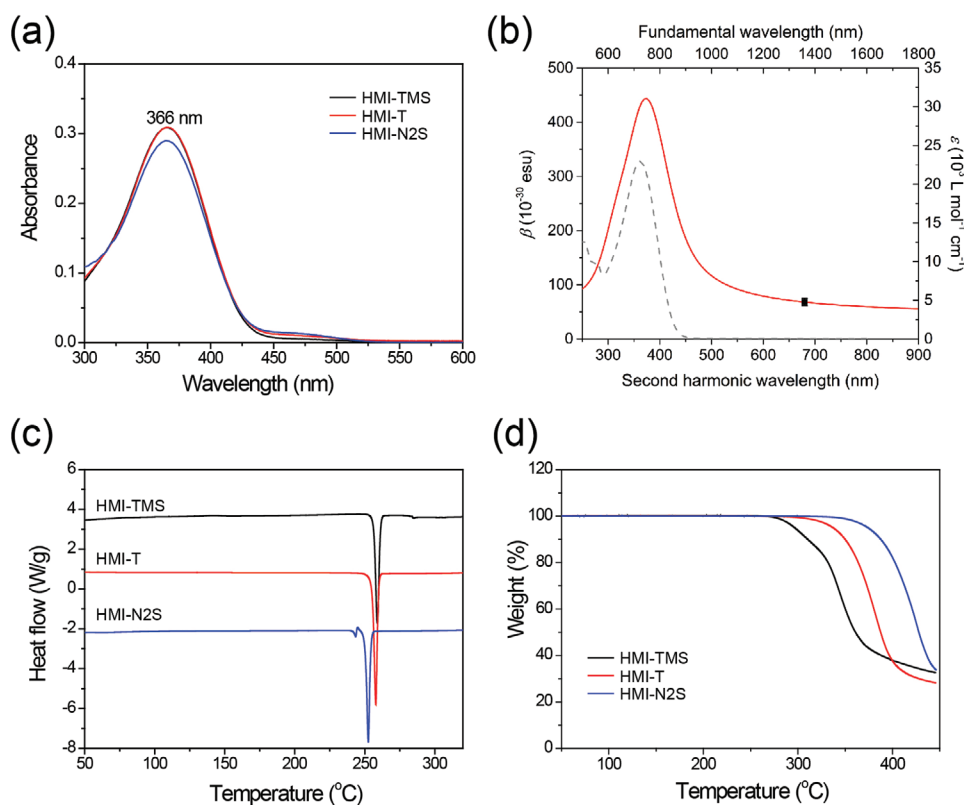


Figure 2. a) UV–vis absorption spectra of the HMI-based crystals in methanol solution. b) Molecular first hyperpolarizability β determined using HRS measurement (square; effective β_{zzz}) and absorption spectrum (dashed line) of the HMI-TMS. c) Differential scanning calorimetry (DSC) and d) thermogravimetric analysis (TGA) thermodiagrams of the HMI-TMS, HMI-T and HMI-N2S crystals.

therefore be considered close to optimum, compared to existing benchmarks, given its short λ_{max} .

The microscopic nonlinearity of wide-bandgap HMI chromophores was also studied using quantum chemical calculations based on the finite-field (FF) approach, as described in Section B in the Supporting Information. The nonresonant hyperpolarizability β_{max} along the main charge-transfer axis of the HMI cation was calculated by considering either the optimized geometry in the gas phase (OPT) or the experimentally determined conformation in the HMI-TMS crystals (EXP). This was then compared with the conventional aniline-type wide-bandgap chromophores (see Table 1).^[36] For the stilbene-type wide-bandgap HMI-TMS, we obtained $\beta_{\text{max}} = 76 \times 10^{-30}$ esu (OPT) and 77×10^{-30} esu (EXP), which are very comparable to the obtained experimental value $\beta_{\text{zzz},0}$. These values were also much larger than those of the aniline-type wide-bandgap chromophores: 16.2, 28.8, 24.1, and 21.9×10^{-30} esu for MNA, NPP, COANP and BNA, respectively (see Table 1).

The large microscopic optical nonlinearity of the HMI cation is related to the electron withdrawing strength of the benzimidazolium group. To evaluate the electron withdrawing strength of the 1,3-dimethyl-1H-benzimidazol-3-ium electron acceptor in the HMI cation, we additionally calculated the maximal first hyperpolarizability β_{max} of the optimized structure (OPT) of the DAI cation, consisting of a 1,3-dimethyl-1H-benzimidazol-3-ium electron acceptor and dimethylamino electron donor. The maximal first hyperpolarizability β_{max} of the DAI (OPT) cation

($\beta_{\text{max}} = 122 \times 10^{-30}$ esu) was slightly lower than that of the cation of the benchmark low-bandgap nonlinear optical crystals with very strong electron-withdrawing groups; e.g., it was $\beta_{\text{max}} = 159 \times 10^{-30}$ esu for the pyridinium-based DAS (4-(4-(dimethylamino)styryl)-1-methylpyridinium) (OPT) cation consisting of the *N*-methyl pyridinium electron acceptor and dimethylamino electron donor in the benchmark DAST crystals.^[37] Therefore, introducing the benzimidazolium electron withdrawing group in the stilbene-type HMI cation simultaneously provides wide-bandgap and large molecular optical nonlinearity, which would not be achievable in the previously reported aniline-type wide-bandgap and benchmark low-bandgap chromophores.

2.3. High Thermal Stability

For conventional wide-bandgap aniline-type chromophores, besides having low molecular optical nonlinearity, the relatively low thermal stability of the crystalline state can be a serious drawback in practical applications. As listed in Table 1, the melting temperature T_m of aniline-type wide-bandgap crystals is relatively low: 133, 116, 73, and 105 °C for MNA, NPP, COANP and BNA, respectively.^[24,29] Figure 2c,d shows differential scanning calorimetry (DSC) and thermogravimetric analysis (TGA) thermodiagrams of the HMI-based crystals, respectively. The HMI-based crystals possess a high melting point above 250 °C, which is interestingly similar to that of the benchmark

stilbene-type low-bandgap nonlinear optical organic crystals and much higher than that of aniline-type wide-bandgap crystals.^[24,29] As a consequence, stilbene-type wide-bandgap HMI chromophores can overcome two of the crucial drawbacks (low molecular optical nonlinearity and low thermal stability) of the aniline-type wide-bandgap chromophores in photonics applications.

2.4. Optimal Chromophore Ordering for Maximal Macroscopic Nonlinearity

To investigate the orientation of the HMI cations in the crystalline state using different counter anions TMS, T and N2S, X-ray single crystal structure analyses were performed on the HMI-TMS, HMI-T and HMI-N2S crystals. Among the three investigated HMI-based crystals, the HMI-TMS and HMI-N2S crystals exhibited noncentrosymmetric molecular ordering with monoclinic Pn and $P2_1$ space groups, respectively, while the HMI-T crystals exhibit centrosymmetric molecular ordering with a monoclinic $P2_1/c$ space group. The molecular packing diagrams of the HMI-TMS, HMI-N2S, and HMI-T crystals are illustrated in Figure 3.

The red solid arrow in Figure 3 indicates the direction of the maximum microscopic first hyperpolarizability β_{\max} of the HMI (EXP) cation in the HMI-TMS crystals. In the HMI-TMS crystals, the HMI cations are almost perfectly aligned, maximizing the diagonal component of the second-order nonlinear optical susceptibility. The molecular ordering angle θ_p between the direction of the first hyperpolarizability β_{\max} of the HMI cation and the polar axis of the HMI-TMS crystal^[12,36] was $\theta_p = 3.0^\circ$ (Figure S4 in the Supporting Information), and the corresponding order parameter of $\cos^3\theta_p = 0.996$ was near the maximum possible practical value (≈ 1.0). In contrast, the molecular ordering angle θ_p of the HMI cation in the HMI-N2S crystals was very large ($\theta_p \approx 83^\circ$), as shown in Figure 3b, and consequently, the order parameter was very small ($\cos^3\theta_p \approx 0.002$). For HMI-T crystals, $\cos^3\theta_p = 0$ due to the centrosymmetric chromophore packing. Therefore, among the three investigated HMI-based crystals, the HMI-TMS crystal, which has the highest order parameter, was determined to be the most suitable for second-order nonlinear optical applications.

HMI-TMS crystals possess a relatively large macroscopic optical nonlinearity. The largest diagonal component of the effective hyperpolarizability tensor of the HMI-TMS crystals,

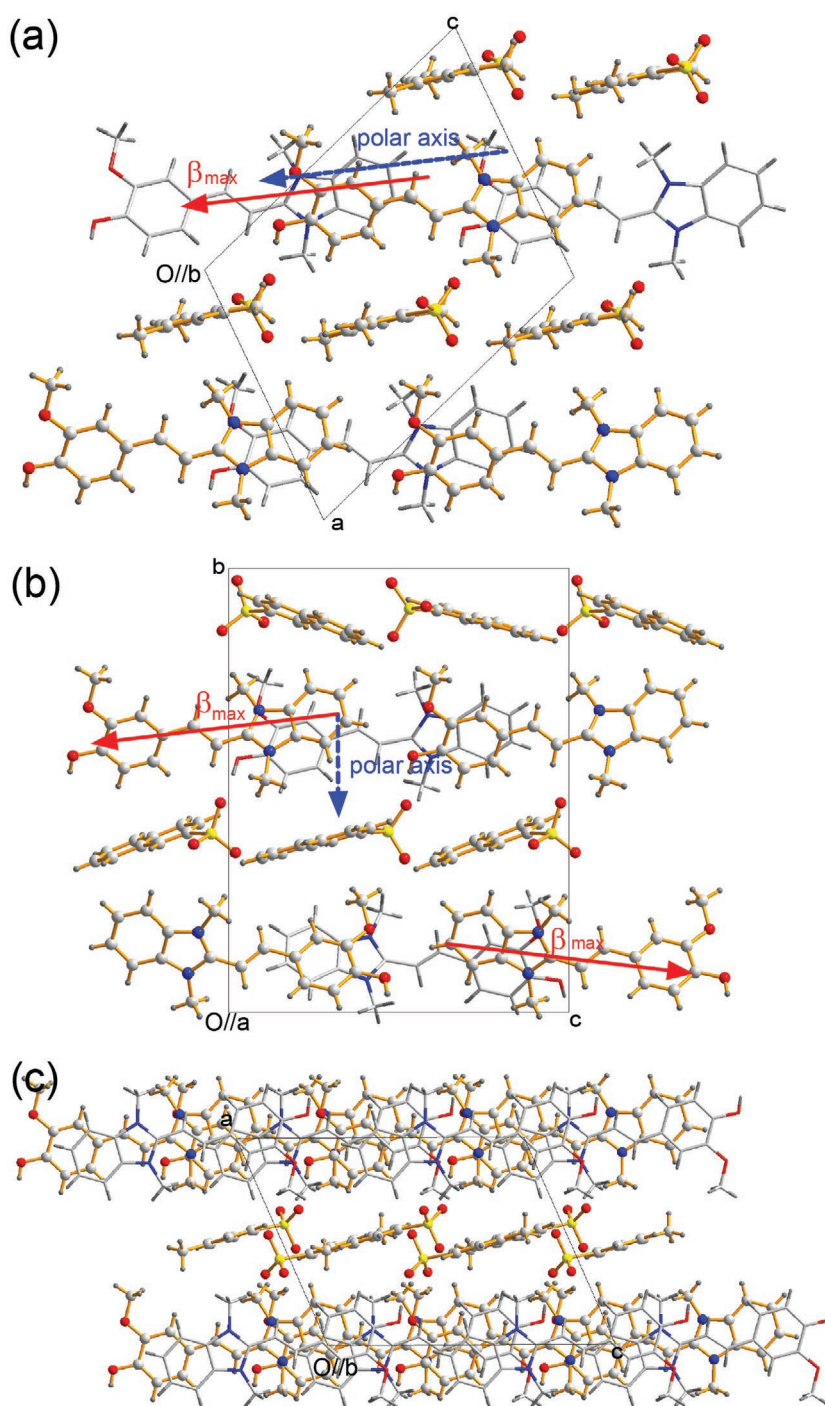


Figure 3. a) Molecular packing diagrams of acentric a) HMI-TMS crystals and b) HMI-N2S crystals projected along the crystallographic b - and a -axes, respectively, and c) centrosymmetric HMI-T crystals projected along the crystallographic b -axis. The directions of the maximal first hyperpolarizability β_{\max} of the HMI cations and the polar axis of the crystals are presented by the red solid and blue dotted arrows, respectively.

evaluated in the oriented-gas model^[38] with the first hyperpolarizability of the HMI (EXP) cation ($\beta_{\max} = 77 \times 10^{-30}$ esu), is $\beta_{111}^{\text{eff}} = 77 \times 10^{-30}$ esu, while all other tensor components are practically zero ($< 2 \times 10^{-30}$ esu). The obtained value for β_{111}^{eff} in the HMI-TMS crystals is reasonable compared to other crystals.

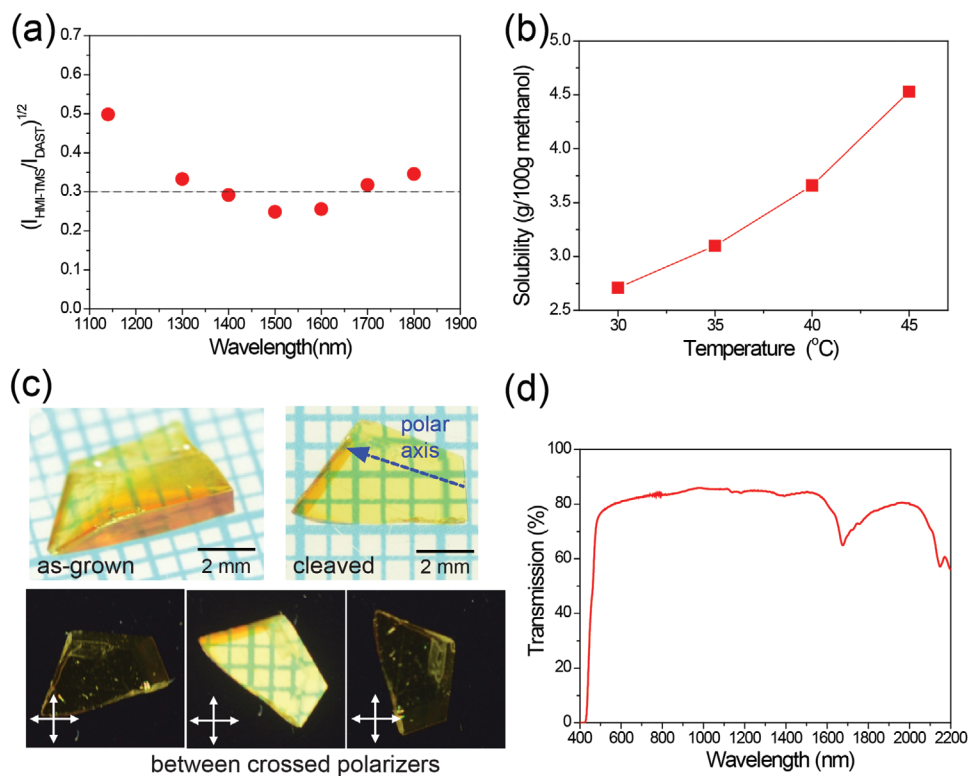


Figure 4. a) Square root of the relative SHG intensity $(I_{\text{HMI-TMS}}/I_{\text{DAST}})^{0.5}$ of the HMI-TMS powder relative to DAST powder at various fundamental wavelengths. b) Solubility of the HMI-TMS crystals in methanol. c) Photographs of the as-grown and cleaved HMI-TMS crystals grown by the slow evaporation method and slow cooling method, respectively, in methanol. The three photographs (bottom) show different orientations of a cleaved HMI-TMS crystal between crossed polarizers. The blue dotted single arrow and the white crossed double arrows indicate the direction of the polar axis and the transmission axes of the polarizers, respectively. d) Transmittance of a 0.24 mm thick cleaved HMI-TMS crystal, measured using unpolarized light.

The ratio of the calculated effective hyperpolarizability tensor of the HMI-TMS crystals relative to the benchmark DAST (4-(4-(dimethylamino)styryl)-1-methylpyridinium 4-methylbenzenesulfonate) crystals^[37] showed good agreement with the results of the powder second harmonic generation (SHG) test.

As shown in **Figure 4a**, the square root of the SHG intensity—which scales with the macroscopic nonlinear optical susceptibility—generated in the HMI-TMS crystals, relative to the DAST crystals, was in the range of 0.25–0.35 at the fundamental wavelengths from 1300 to 1800 nm. The ratio obtained from the SHG experiment is roughly proportional to the effective hyperpolarizability tensor. More precisely, the square root of SHG efficiency, neglecting eventual phase-matching enhancements and intermolecular interactions, was proportional to the factor $N\sqrt{\langle(\beta^{\text{eff}})^2\rangle}$, where N is the number density of chromophores, and $\langle(\beta^{\text{eff}})^2\rangle$ denotes the spatial average over all effective hyperpolarizability tensor components, when the off-diagonal components are also considered.^[12,39] The calculated (nonresonant) ratio between the factors $N\sqrt{\langle(\beta^{\text{eff}})^2\rangle}$ for HMI-TMS and DAST^[12] equaled 0.38, which is in excellent agreement with the SHG measurement presented in **Figure 4a**.

The macroscopic nonlinear optical susceptibility $\chi^{(2)}$ is proportional to the product of the effective hyperpolarizability tensor β_{ijk}^{eff} and the number density N of chromophores in the crystalline state. The largest diagonal component $N\beta_{111}^{\text{eff}}$ of the HMI-TMS crystals was remarkably larger than that of the aniline-type wide-bandgap nonlinear optical crystals

(see **Table 1**). For example, the diagonal component $N\beta_{111}^{\text{eff}}$ of the HMI-TMS crystals (124×10^{-3} esu m^{-3}) was one order of magnitude larger than that of NPP ($N\beta_{222}^{\text{eff}} = 11.2$ esu m^{-3}). Note that in many wide-bandgap nonlinear organic crystals, the calculated maximal diagonal component of the effective hyperpolarizability tensor is smaller than the maximal off-diagonal component (see **Table 1**). This is due to the larger molecular ordering angle θ_p in most of these crystals. This is in agreement with the reported experimental values; for example, $d_{222} = 16.8$ pm V^{-1} and $d_{211} = 51$ pm V^{-1} for NPP crystals and $d_{333} = 13.7$ pm V^{-1} and $d_{322} = 32$ pm V^{-1} for COANP crystals at 1064 nm.^[24,40] As a result, compared to aniline-type wide-bandgap crystals, the stilbene-based wide-bandgap HMI-TMS crystals with their large macroscopic optical nonlinearity and high thermal stability can be considered beneficial for practical applications.

2.5. Excellent Crystal Characteristics for Optical Applications

HMI-TMS exhibits relatively high solubility in methanol, as shown in **Figure 4b**. Bulk HMI-TMS single crystals were grown using solution growth methods. **Figure 4c** shows photographs of the as-grown and cleaved HMI-TMS crystals. The HMI-TMS crystals prepared by the simple cleaving method^[20] exhibited uniform transmission, as confirmed by inspection through crossed polarizers. The polar axis of the HMI-TMS crystal was along the largest cleaved surface (see the blue dotted

arrow in Figure 4c), which is optimal for free-space THz wave generation.

As expected from the solution data for the wide-bandgap HMI cations, the HMI-TMS crystals showed a relatively low cut-off absorption wavelength; the 0.24 mm thick HMI-TMS crystal showed a wide transparency from 480 to 1550 nm (Figure 4d). Consequently, the HMI-TMS single crystals, with excellent crystal morphology and a large transparency range, large macroscopic nonlinear optical susceptibility and high thermal stability, are very promising candidates for efficient optical-to-THz conversion with near-IR pumping, as will be discussed in the following section.

2.6. Efficient Optical-to-THz Conversion with Improved Phase Matching

To investigate the THz wave generation characteristics of wide-bandgap HMI-TMS crystals, THz experiments were performed, employing 1 kHz femtosecond pump pulses both at 800 and 1300 nm with pulse durations of 100 and 150 fs, respectively.^[8] Both pump pulses were loosely focused on the crystal. The spot diameter was 1.5 mm. THz waves were generated by optical rectification in a 0.70 mm thick HMI-TMS crystal and subsequently detected by the electro-optic sampling (EOS) method in a 0.30 mm thick GaP crystal. For comparison, a benchmark organic crystal, 0.79 mm thick HMQ-TMS, and a benchmark inorganic crystal, 1.0 mm thick ZnTe, were also examined under the same experimental conditions. The details of our

THz wave generation setup are described in Section C in the Supporting Information.

Figure 5a–c and Figure S5 in the Supporting Information show the results of the THz wave generation experiments. The 0.70 mm thick HMI-TMS crystal provided high optical-to-THz conversion efficiency. We obtained up to 1.6 times higher peak-to-peak THz electric field than with the 1.0 mm thick ZnTe crystal (Figure 5a), which was perfectly phase-matchable at 800 nm.^[9a–c] Under the phase matching condition, the generated THz electric field is proportional to crystal thickness.^[7d,19] The optical-to-THz conversion efficiency of the 0.7 mm thick HMI-TMS was up to 2.3 times higher than that of ZnTe normalized to the same crystal thickness.

Interestingly, although the wide-bandgap HMI-TMS crystals (calculated $\beta_{111}^{\text{eff}} = 77 \times 10^{-30}$ esu; experimental static first hyperpolarizability $\beta_{zzz,0} = 47 \times 10^{-30}$ esu) exhibited only about 42% of the macroscopic (or 56% of the experimental microscopic) optical nonlinearity of the benchmark low-bandgap HMQ-TMS crystals (calculated $\beta_{333}^{\text{eff}} = 185 \times 10^{-30}$ esu;^[20] experimental static first hyperpolarizability of HMQ cation $\beta_{zzz,0} = 84 \times 10^{-30}$ esu in acetonitrile^[41]) the peak-to-peak THz electric field obtained with the 0.70 mm thick HMI-TMS crystal pumped at 800 nm was comparable to the one generated from the benchmark 0.79 mm thick HMQ-TMS crystal, as shown in Figure 5a and the left side of Figure 5c.

In contrast, at a pump wavelength of 1300 nm, the generated peak-to-peak THz electric field of the 0.70 mm thick HMI-TMS crystal was about 50% of the one obtained with the 0.79 mm thick HMQ-TMS crystal. This is well matched to the ratio of

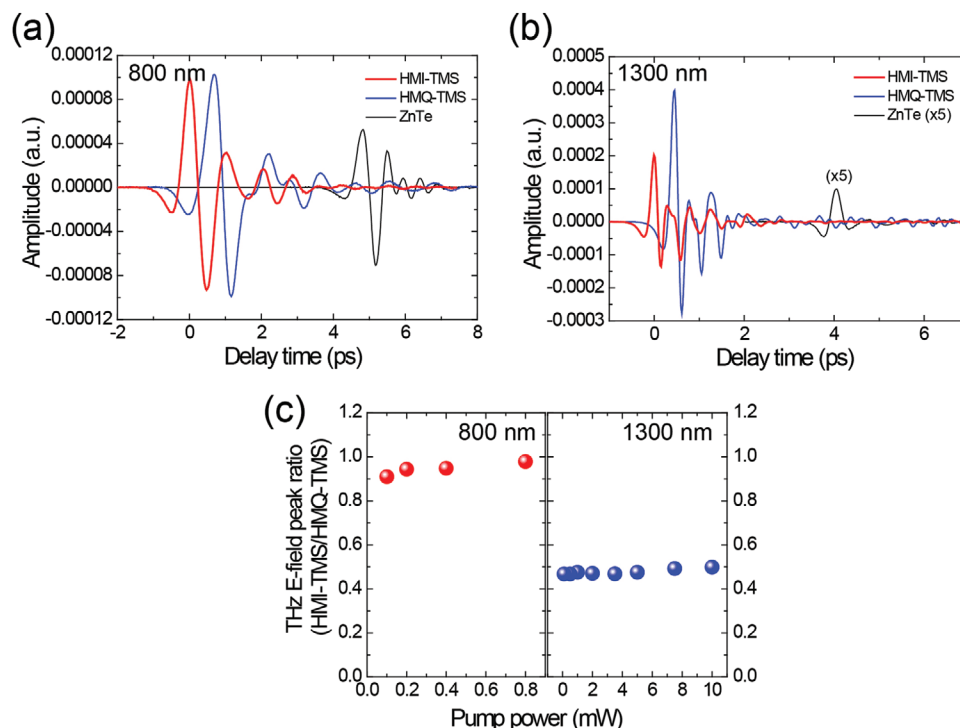


Figure 5. THz wave generation experiments with 0.70 mm thick HMI-TMS, 0.79 mm thick HMQ-TMS and 1.0 mm thick ZnTe crystals. Measured time traces when pumped at a) 800 nm with an average pump power of 0.8 mW (corresponding to a pump fluence of $45.27 \mu\text{J cm}^{-2}$) and at b) 1300 nm with an average pump power of 10 mW (corresponding to a pump fluence of $565.9 \mu\text{J cm}^{-2}$). c) Ratio of peak-to-peak THz electric field of a HMI-TMS crystal relative to that of a HMQ-TMS crystal as a function of pump power in the linear power response range (see Figure S5 in the Supporting Information).

the macroscopic and microscopic optical nonlinearities (42% and 56%) (see Figure 5c). This clearly indicates that the wide-bandgap HMI-TMS crystals probably provide better phase matching compared to the benchmark low-bandgap HMQ-TMS crystals when pumped at 800 nm.

In order to clarify the interesting behavior of the HMI-TMS crystals during THz wave generation at 800 nm, the refractive indices of the HMI-TMS crystals in both optical and THz frequency ranges were measured, as described in Section C in the Supporting Information. Figure 6a,b shows the measured optical group index and the THz phase index of the HMI-TMS crystals. Compared to the HMQ-TMS crystals,^[42] the optical group index of the HMI-TMS crystals was substantially smaller, as shown in Figure 6a: the optical group indices were 2.14 and 2.41 for the HMI-TMS and HMQ-TMS crystals, respectively, at 800 nm. When the wavelength increased, the difference in the optical group indices of the HMI-TMS and HMQ-TMS crystals became smaller. At the longer IR wavelength of 1500 nm, the optical group indices were 1.95 and 2.0 for the HMI-TMS and HMQ-TMS crystals, respectively. In the THz frequency region, the refractive index of the HMI-TMS crystals was still smaller than that of the HMQ-TMS crystals,^[16,42] by about the same amount as near 1500 nm (more details are presented in Figure S6 in the Supporting Information).

In particular, as shown in Figure 6b, the relevant refractive index difference $\Delta n = n_{g,opt} - n_{THz}$ of the HMI-TMS crystals below 1000 nm was very small, as well as around 1200–1600 nm; i.e., the phase matching condition was well satisfied across the wide pump wavelengths in the near-IR region, except for an oscillation region in the optical group index around 1000 nm. These phase matching characteristics of the HMI-TMS crystals are interesting, because most benchmark organic crystals show poor phase matching at near-IR wavelengths below 1000 nm. The improved phase matching characteristics of the HMI-TMS crystals results in a high optical-to-THz conversion efficiency at 800-nm pumping.

To illustrate the phase matching condition at various pump wavelengths λ and generated THz frequencies ν , the coherence length $l_c(\lambda, \nu) = c/(2\nu\Delta n)$ of the HMI-TMS crystals was calculated, as shown in Figure 6c. Compared to the equivalent coherence-length plot of the HMQ-TMS crystals reported in ref. [16], the HMI-TMS crystals indeed showed better phase matching (i.e., much longer coherence length), particularly at near-IR pump wavelengths around 800 nm. Consequently, this work successfully demonstrates the proof-of-principle of refractive index engineering using the wide-bandgap approach, in which wide-bandgap HMI chromophores were introduced to reduce the optical group index. This led to substantially improved

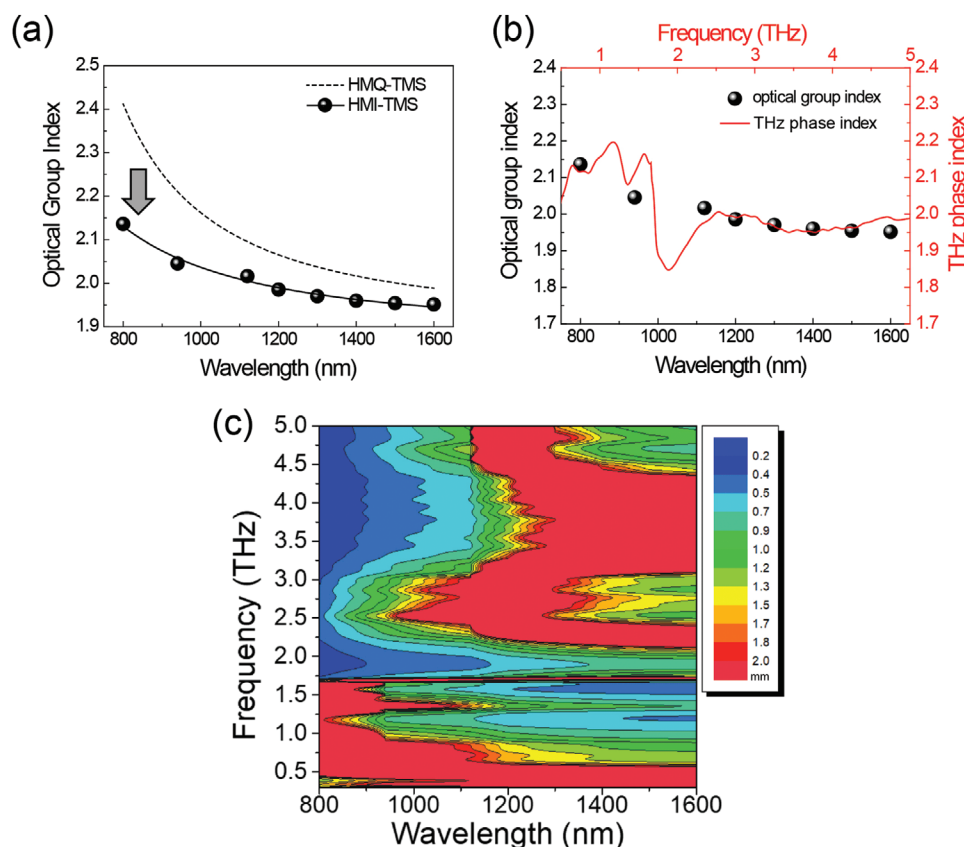


Figure 6. a) Optical group indices of the HMI-TMS and low-bandgap HMQ-TMS crystals. The black solid line is from a single-oscillator Sellmeier model best fit to the experimental data. The optical group index of the HMQ-TMS crystals (black dashed curve) is according to the literature.^[41] b) Optical group index (black solid circles) and THz phase index (solid red curves). c) Coherence length as a function of the pump wavelength and the generated THz frequency of HMI-TMS crystals.

phase matching conditions and efficient THz wave generation by pumping at the technologically important wavelength.

Note that HMI-TMS crystal pumped at the longer IR wavelength of 1300 nm exhibited a generated THz wave with a broad spectral bandwidth and an upper cut-off frequency of ≈ 8 THz, as shown in Figure S5d in the Supporting Information. Although the HMI-TMS crystals provided a better phase matching condition around 800 nm compared to the HMQ-TMS crystals, the spectral bandwidth of the generated THz wave of the HMI-TMS crystals at near-IR wavelengths is still limited as shown in Figure S5b in the Supporting Information. This is because HMI-TMS crystals pumped at this wavelength are better phase matchable in the lower THz frequency region (≤ 2 THz, see Figure 6c), while at IR wavelengths near 1300 nm that are better phase matched in the higher THz frequency region. Consequently, the generated THz spectral bandwidth of HMI-TMS crystals pumped at 1300 nm is much broader than at 800 nm, similar to benchmark organic THz generators (Figure S5b,d in the Supporting Information).

As shown in Figure S5e,f in the Supporting Information, the generated THz field amplitude in the HMI-TMS crystal linearly increases when the input power of the fundamental pump beam is increased (see yellow highlighted region), as expected for optical rectification processes in the undepleted pump approximation regime.^[15,19] However, the linearity between the generated THz electric field and the pump power is lost at a certain fluence level; e.g., $45.27 \mu\text{J cm}^{-2}$ at 800 nm and $565.9 \mu\text{J cm}^{-2}$ at 1300 nm in the 0.70 mm thick HMI-TMS crystal. The transition point from the linear to nonlinear relationship varies depending on different experimental conditions (e.g., crystal thickness). Note that this deviation from the linear dependence may result from (reversible) photoswitching of the molecules at high pump powers, which was also observed for HMI-TMS in solution (see Figure S8 in the Supporting Information). Our on-going work will involve chemical modification of the large-bandgap benzimidazolium-based cation to prevent undesired competing photoinduced processes, which limit the THz conversion efficiency at higher pump fluences.^[43]

2.7. Discussion on Wide-Bandgap Approach

In this work, we propose introducing wide-bandgap chromophores into crystals as an efficient design concept to reduce the refractive index in the near-IR region, especially below 1000 nm, which leads to better phase matching for THz wave generation in a wide spectral range. The present work is mainly focused on refractive index engineering, based on a unique method of chemically modifying chromophores. This approach was realized with the newly designed stilbene-type wide-bandgap HMI-TMS crystal, which was modified from benchmark stilbene-type low-bandgap HMQ-TMS crystals. Compared to the mother HMQ-TMS crystal, the HMI-TMS crystal exhibited much lower refractive indices while maintaining other desired physical properties: e.g., overall molecular ordering features (i.e., perfectly parallel alignment of nonlinear optical cationic chromophores to maximize macroscopic optical nonlinearity) and high thermal stability. Up to now, methods of predicting and screening the refractive index of organic crystals have only

been addressed by quantum chemical calculations, even with known crystal structures.^[44]

In addition, in the THz region, stilbene-type HMI-TMS crystals exhibited similar absorption characteristics as mother HMQ-TMS crystals. As shown in Figure S7 in the Supporting Information, the HMI-TMS crystals exhibit a relatively low absorption coefficient in the THz region below 5 THz. Moreover, the THz absorption spectrum of the HMI-TMS crystal was very similar to the benchmark HMQ-TMS crystals^[16,42] because both the HMI and HMQ chromophores consist of a similar stilbene-type π -conjugated structure. As a result, we were able to demonstrate a wide-bandgap approach to efficient THz wave generation, by simultaneously maintaining the low amplitude molecular vibrational modes in the THz region, which is important to prevent self-absorption of the generated THz waves.

In addition to successfully demonstrating refractive index engineering of organic nonlinear crystals, we found the newly designed wide-bandgap stilbene-type HMI-TMS crystals were very interesting for THz wave generation. Although the HMI-TMS crystals pumped at IR wavelength delivered half the THz generation efficiency of benchmark mother HMQ-TMS crystals, this efficiency from HMI-TMS crystal is still very high. The peak-to-peak THz electric field was one order of magnitude higher than that generated from an inorganic ZnTe crystal when pumped at 1300 nm with the same pump fluence of $565.9 \mu\text{J cm}^{-2}$ (Figure 5b). Furthermore, the HMI-TMS crystals showed generated THz waves with broad spectral bandwidths and an upper cut-off frequency of ≈ 8 THz (Figure S5d in the Supporting Information).

In particular, at the technologically important pump wavelength of 800 nm, the HMI-TMS crystals exhibited excellent THz wave generation efficiency. The wide-bandgap stilbene-type HMI-TMS crystals pumped at 800 nm exhibited the same order of magnitude THz wave generation efficiency as the benchmark low-bandgap stilbene-type HMQ-TMS crystals pumped at 800 nm shown in this work and benchmark wide-bandgap aniline-type BNA and COANP crystals pumped at 815 and 776 nm, respectively.^[46,47] Note that the ideal pump wavelength for phase matching in ZnTe is located near 800 nm.^[9a-c]

Despite their THz generation characteristics, the physical properties of the HMI-TMS crystals still need improvements. The thermal stability of the stilbene-type HMI-TMS crystals is higher than aniline-type crystals, as discussed above in Section 2.3. However, due to ionic characteristics of the HMI-TMS crystals, environmental instability caused by high humidity (or water-rich environment) may occur over long-term periods, which may not be the case in nonionic crystals. On the other hand, the ionic HMI-TMS crystals might possess higher sublimation temperatures compared to some nonionic crystals with low melting temperatures. Furthermore, undesired photoinduced processes in the HMI-TMS crystals, which are more often observed in two aromatic ring systems than one aromatic ring systems, should be improved.

3. Conclusions

We have successfully demonstrated refractive index engineering using a wide-bandgap approach, based on

benzimidazolium-based HMI-TMS crystals. We achieved efficient THz wave generation, due to improved phase matching, with pumping at near-IR wavelengths of around 800 nm. The stilbene-type HMI cations exhibited a very low wavelength of maximum absorption of only 364 nm in methanol solution. The HMI-TMS crystals provided high optical-to-THz conversion efficiency at 800 nm with better phase matching due to the much lower near-IR refractive index, compared to benchmark HMQ-TMS crystals. The refractive index engineering of optical materials based on the wide-bandgap approach is a very promising strategy for diverse applications, including efficient optical-to-THz frequency conversion, and controlling the refractive index of π -conjugated organic materials. To extend the proposed wide-bandgap approach, further chemical modification will be required to optimize the bandgap (and refractive index) and enhance macroscopic optical nonlinearity.

4. Experimental Section

Synthesis: The HMI-based compounds HMI-TMS, HMI-T, and HMI-N2S were synthesized by a condensation reaction of vanillin, including electron-donor groups and a corresponding intermediate (1,2,3-trimethyl-1H-benzimidazol-3-ium with corresponding aromatic sulfonate) including benzimidazolium-based electron acceptor groups, according to the literature.^[20,30a] Since the benzimidazolium-based intermediates, such as 2,3-dimethyl-1H-benzimidazol-3-ium and 2-methyl-1H-benzimidazol-3-ium, could not be purely separated from the byproducts by precipitation and/or recrystallization methods, the mixture of benzimidazolium-based intermediates and byproducts was used for the condensation reaction of vanillin.

2-(4-Hydroxy-3-methoxystyryl)-1,3-Dimethyl-Benzimidazolium 2,4,6-Trimethylbenzenesulfonate (HMI-TMS): ¹H NMR (600 MHz, DMSO-*d*₆, δ): 9.90 (s, 1H, -OH), 8.01 (m, 2H, C₆H₄), 7.72 (d, *J* = 16.8 Hz, 1H, CH), 7.66 (m, 2H, C₆H₄), 7.54 (s, 1H, C₆H₃), 7.36 (m, 1H, C₆H₃), 7.35 (d, *J* = 16.2 Hz, 1H, CH), 6.91 (d, *J* = 7.8 Hz, 1H, C₆H₃), 6.73 (s, 2H, C₆H₂SO₃⁻), 4.12 (s, 6H, N₂C₂H₆), 3.89 (s, 3H, OCH₃), 2.48 (s, 6H, C₂H₆), 2.16 (s, 3H, CH₃). ¹³C NMR (600 MHz, DMSO-*d*₆, δ): 150.90, 149.39, 148.68, 147.65, 143.51, 136.58, 136.38, 132.49, 130.29, 126.72, 126.50, 124.49, 116.25, 113.30, 112.08, 104.46, 56.49, 33.36, 23.26, 20.80. Elemental analysis for C₂₇H₃₀N₂O₅S: Calcd. C 65.57, H 6.11, N 5.66, S 6.48; Found: C 65.53, H 6.14, N 5.66, S 6.46.

2-(4-Hydroxy-3-Methoxystyryl)-1,3-Dimethyl-Benzimidazolium 4-Methylbenzenesulfonate (HMI-T): ¹H NMR (600 MHz, DMSO-*d*₆, δ): 9.87 (s, 1H, -OH), 8.01 (m, 2H, C₆H₄), 7.72 (d, *J* = 16.8 Hz, 1H, CH), 7.66 (m, 2H, C₆H₄), 7.55 (s, 1H, C₆H₃), 7.46 (d, *J* = 8.4 Hz, 2H, C₆H₄SO₃⁻), 7.37 (m, 1H, C₆H₃), 7.34 (m, 1H, CH), 7.09 (d, *J* = 7.2 Hz, 2H, C₆H₄SO₃⁻), 6.91 (d, *J* = 8.4 Hz, 1H, C₆H₃), 4.12 (s, 6H, N₂C₂H₆), 3.89 (s, 3H, OCH₃), 2.28 (s, 3H, CH₃). ¹³C NMR (600 MHz, DMSO-*d*₆, δ): 150.85, 149.39, 148.67, 147.65, 146.46, 138.00, 132.50, 128.52, 126.73, 126.53, 126.01, 124.48, 116.24, 113.31, 112.07, 104.50, 56.49, 33.37, 21.29. Elemental analysis for C₂₅H₂₆N₂O₅S: Calcd. C 64.36, H 5.62, N 6.00, S 6.87; found: C 64.34, H 5.61, N 5.99, S 6.78.

2-(4-Hydroxy-3-Methoxystyryl)-1,3-Dimethyl-Benzimidazolium Naphthalene-2-Sulfonate (HMI-N2S): ¹H NMR (600 MHz, DMSO-*d*₆, δ): 9.91 (s, 1H, -OH), 8.12 (s, 1H, C₁₀H₇SO₃⁻), 8.01 (m, 2H, C₆H₄), 7.95 (m, 1H, C₁₀H₇SO₃⁻), 7.88 (m, 1H, C₁₀H₇SO₃⁻), 7.84 (d, *J* = 8.4 Hz, 1H, C₁₀H₇SO₃⁻), 7.72 (d, *J* = 16.2 Hz, 1H, CH), 7.70 (m, 1H, C₁₀H₇SO₃⁻), 7.66 (m, 2H, C₆H₄), 7.55 (s, 1H, C₆H₃), 7.51 (m, 2H, C₁₀H₇SO₃⁻), 7.36 (m, 1H, C₆H₃), 7.34 (d, *J* = 16.2 Hz, 1H, CH), 6.90 (d, *J* = 7.8 Hz, 1H, C₆H₃), 4.11 (s, 6H, N₂C₂H₆), 3.89 (s, 3H, OCH₃). ¹³C NMR (600 MHz, DMSO-*d*₆, δ): 150.98, 149.39, 148.70, 147.65, 146.33, 133.20, 132.69, 132.50, 128.94, 127.96, 127.75, 126.88, 126.76, 126.72, 126.46, 124.56, 124.51, 116.27, 113.30, 112.07, 104.40, 56.49, 33.36, 31.21. Elemental analysis for C₂₈H₂₆N₂O₅S:

Calcd. C 66.91, H 5.21, N 5.57, S 6.38; Found: C 66.97, H 5.22, N 5.52, S 6.40.

X-Ray Crystal Structure Analysis: The stilbene-type wide-bandgap single crystals (HMI-TMS, HMI-N2S, and HMI-T) were grown by the rapid cooling method in methanol for X-ray single crystal structure analysis.

HMI-TMS: C₂₇H₃₀N₂O₅S, *M_r* = 494.59, Monoclinic, space group *Pn*, *a* = 11.4249(6) Å, *b* = 8.0033(5) Å, *c* = 14.3812(8) Å, β = 108.709(1)°, *V* = 1245.49(12) Å³, *Z* = 2, *T* = 290(1) K, μ (MoK α) = 0.171 mm⁻¹. Of 6523 reflections collected in the θ range 2.99°–27.415° using ω scans on a Rigaku R-axis Rapid S diffractometer, 5090 were unique reflections (*R*_{int} = 0.0575). The structure was solved and refined against *F*² using SHELXL-2014/7,^[45] 323 variables, ωR_2 = 0.1515, *R*₁ = 0.0617 (*F*² > 2 σ (*F*²)), GOF = 0.994, and max/min residual electron density 0.252/–0.194 e Å⁻³. CCDC-1848730.

HMI-N2S: C₂₈H₂₆N₂O₅S, *M_r* = 502.57, Monoclinic, space group *P2*₁, *a* = 7.9260(2) Å, *b* = 20.0022(5) Å, *c* = 15.3143(5) Å, β = 90.9733(9)°, *V* = 2427.54(12) Å³, *Z* = 4, *T* = 150(1) K, μ (MoK α) = 0.177 mm⁻¹. Of 21 003 reflections collected in the θ range 3.05°–27.46° using ω scans on a Rigaku R-axis Rapid S diffractometer, 10 316 were unique reflections (*R*_{int} = 0.0250). The structure was solved and refined against *F*² using SHELXL-2014/7,^[45] 657 variables, ωR_2 = 0.1431, *R*₁ = 0.0529 (*F*² > 2 σ (*F*²)), GOF = 1.052, and max/min residual electron density 1.279/–0.429 e Å⁻³. CCDC-1848731.

HMI-T: C₂₅H₂₆N₂O₅S, *M_r* = 466.54, Monoclinic, space group *P2*₁/*c*, *a* = 11.9188(6) Å, *b* = 13.6264(10) Å, *c* = 15.1091(7) Å, β = 113.5960(10)°, *V* = 2248.7(2) Å³, *Z* = 4, *T* = 290(1) K, μ (MoK α) = 0.185 mm⁻¹. Of 17 088 reflections collected in the θ range 3.159°–24.997° using ω scans on a Rigaku R-axis Rapid S diffractometer, 3921 were unique reflections (*R*_{int} = 0.0392). The structure was solved and refined against *F*² using SHELXL-2014/7,^[45] 304 variables, ωR_2 = 0.1878, *R*₁ = 0.0541 (*F*² > 2 σ (*F*²)), GOF = 1.149, and max/min residual electron density 0.583/–0.599 e Å⁻³. CCDC-1855375.

Supporting Information

Supporting Information is available from the Wiley Online Library or from the author.

Acknowledgements

D.J.K. and W.T.K. contributed equally to this work. This work has been supported by the National Research Foundation of Korea (NRF) funded by the Ministry of Science, ICT & Future Planning, Korea (Nos. 2019K1A3A1A14057973, 2014R1A5A1009799, 2019R1A2C3003504, and 2020R1A4A2002828), Swiss National Science Foundation (SNSF), Switzerland (No. IZKSZ2_188194) and the Fund for Scientific Research-Flanders (FWO; Projects No. G020612N, G052213N, G035918N, G036618N, and the EOS CHARMING project G0F6218N [EOS-ID 30467715]).

Conflict of Interest

The authors declare no conflict of interest.

Keywords

electro-optical materials, nonlinear optics, terahertz photonics

Received: December 16, 2019

Revised: February 26, 2020

Published online:

- [1] a) T. Kampfrath, K. Tanaka, K. A. Nelson, *Nat. Photonics* **2013**, 7, 680; b) C. Vicario, C. Ruchert, F. Ardana-Lamas, P. M. Derlet, B. Tudu, J. Luning, C. P. Hauri, *Nat. Photonics* **2013**, 7, 720.
- [2] a) R. L. Milot, M. T. Klug, C. L. Davies, Z. Wang, H. Kraus, H. J. Snaith, M. B. Johnston, L. M. Herz, *Adv. Mater.* **2018**, 30, 1804506; b) H. Jung, J. Koo, E. Heo, B. Cho, C. In, W. Lee, H. Jo, J. H. Cho, H. Choi, M. S. Kang, H. Lee, *Adv. Mater.* **2018**, 30, 1802760; c) E. P. J. Parrott, J. A. Zeitler, J. McGregor, S.-P. Oei, H. E. Unalan, W. I. Milne, J.-P. Tessonier, D. S. Su, R. Schlögl, L. F. Gladden, *Adv. Mater.* **2009**, 21, 3953; d) K. L. Nguyen, T. Frišić, G. M. Day, L. F. Gladden, W. Jones, *Nat. Mater.* **2007**, 6, 206; e) F. Perakis, L. D. Marco, A. Shalit, F. Tang, Z. R. Kann, T. D. Kühne, R. Torre, M. Bonn, Y. Nagata, *Chem. Rev.* **2016**, 116, 7590.
- [3] a) X. Yang, X. Zhao, K. Yang, Y. Liu, Y. Liu, W. Fu, Y. Luo, *Trends Biotechnol.* **2016**, 34, 810; b) R. Ulbricht, E. Hendry, J. Shan, T. F. Heinz, M. Bonn, *Rev. Mod. Phys.* **2011**, 83, 543; c) J. B. Baxter, G. W. Guglietta, *Anal. Chem.* **2011**, 83, 4342; d) S. S. Dhillon, M. S. Vitiello, E. H. Linfield, A. G. Davies, M. C. Hoffmann, J. Booske, C. Paoloni, M. Gensch, P. Weightman, G. P. Williams, E. Castro-Camus, D. R. Cumming, F. Simoens, I. Escorcia-Carranza, J. Grant, S. Lucyszyn, M. Kuwata-Gonokami, K. Konishi, M. Koch, C. A. Schmuttenmaer, T. L. Cocker, R. Huber, A. G. Markelz, Z. D. Taylor, V. P. Wallace, J. Axel Zeitler, J. Sibik, T. M. Korter, B. Ellison, S. Rea, P. Goldsmith, K. B. Cooper, R. Appleby, D. Pardo, P. G. Huggard, V. Krozer, H. Shams, M. Fice, C. Renaud, A. Seeds, A. Stühr, M. Naftaly, N. Ridler, R. Clarke, J. E. Cunningham, M. B. Johnston, *J. Phys. D: Appl. Phys.* **2017**, 50, 043001; e) W. Zouaghi, M. D. Thomson, K. Rabia, R. Hahn, V. Blank, H. G. Roskos, *Eur. J. Phys.* **2013**, 34, S179; f) M. Walther, B. M. Fischer, A. Ortner, A. Bitzer, A. Thoman, H. Helm, *Anal. Bioanal. Chem.* **2010**, 397, 1009.
- [4] J. A. Fülöp, S. Tzortzakakis, T. Kampfrath, *Adv. Opt. Mater.* **2020**, 8, 1900681.
- [5] J. Shi, Z. Li, D. K. Sang, Y. Xiang, J. Li, S. Zhang, H. Zhang, *J. Mater. Chem. C* **2018**, 6, 1291.
- [6] a) M. Tonouchi, *Nat. Photonics* **2007**, 1, 97; b) B. Ferguson, X.-C. Zhang, *Nat. Mater.* **2002**, 1, 26; c) X. Zheng, C. V. Mclaughlin, P. Cunningham, L. M. Hayden, *J. Nanoelectron. Optoelectron.* **2007**, 2, 58; d) R. A. Lewis, *J. Phys. D: Appl. Phys.* **2014**, 47, 374001.
- [7] a) S. H. Lee, J. Lu, S. J. Lee, J. H. Han, C. U. Jeong, S. C. Lee, X. Li, M. Jazbinsek, W. Yoon, H. Yun, B. J. Kang, F. Rotermund, K. A. Nelson, O. P. Kwon, *Adv. Mater.* **2017**, 29, 1701748; b) G. A. Valdivia-Berroeta, L. K. Heki, E. A. McMurray, L. A. Foote, S. H. Nazari, L. Y. Serafin, S. J. Smith, D. J. Michaelis, J. A. Johnson, *Adv. Opt. Mater.* **2018**, 6, 1800383; c) U. Venkataramudu, C. Sahoo, S. Leelashree, M. Venkatesh, D. Ganesh, S. R. G. Naraharisetty, A. K. Chaudhary, S. Srinath, R. Chandrasekar, *J. Mater. Chem. C* **2018**, 6, 9330; d) M. Savoini, L. Huber, H. Cuppen, E. Abreu, M. Kubel, M. J. Neugebauer, Y. Duan, P. Beaud, J. Xu, T. Rasing, S. L. Johnson, *ACS Photonics* **2018**, 5, 671; e) K. Thirupugamani, M. Venkatesh, S. Karthick, K. K. Maurya, N. Vijayan, A. K. Chaudhary, S. Brahadeeswaran, *CrystEngComm* **2017**, 19, 2623; f) B. Liu, H. Bromberger, A. Cartella, T. Gebert, M. Först, A. Cavalleri, *Opt. Lett.* **2017**, 42, 129; g) X. Zhang, X. Jiang, P. Liu, Y. Li, H. Tu, Z. Lin, D. Xu, G. Zhang, Y. Wu, J. Yao, *CrystEngComm* **2016**, 18, 3667.
- [8] B. J. Kang, S. H. Lee, W. T. Kim, S. C. Lee, K. Lee, G. Benacchio, G. Montemezzani, M. Jazbinsek, O. P. Kwon, F. Rotermund, *Adv. Funct. Mater.* **2018**, 28, 1707195.
- [9] a) F. Blanchard, L. Razzari, H. C. Bandulet, G. Sharma, R. Morandotti, J. C. Kieffer, T. Ozaki, M. Reid, H. F. Tiedje, H. K. Haugen, F. A. Hegmann, *Opt. Express* **2007**, 15, 13212; b) J. Ahn, A. Efimov, R. Averitt, A. Taylor, *Opt. Express* **2003**, 11, 2486; c) G. Chang, C. J. Divin, C. H. Liu, S. L. Williamson, A. Galvanauskas, T. B. Norris, *Opt. Lett.* **2007**, 32, 433; d) F. Blanchard, X. Ropagnol, H. Hafez, H. Razavipour, M. Bolduc, R. Morandotti, T. Ozaki, D. G. Cooke, *Opt. Lett.* **2014**, 39, 4333; e) J. A. Fülöp, L. Pálfalvi, G. Almási, J. Hebling, *Opt. Express* **2010**, 18, 12311.
- [10] a) Y. Wu, M. Elyasi, X. Qiu, M. Chen, Y. Liu, L. Ke, H. Yang, *Adv. Mater.* **2017**, 29, 1603031; b) B. Güzelturk, R. A. Belisle, M. D. Smith, K. Bruening, R. Prasanna, Y. Yuan, V. Gopalan, C. J. Tassone, H. I. Karunadasa, M. D. McGehee, A. M. Lindenberg, *Adv. Mater.* **2018**, 30, 1704737; c) I. C. Sandall, N. E. Porter, M. Wagner, H. Schneider, S. Winnerl, M. Helm, L. Wilson, *Appl. Phys. Lett.* **2010**, 96, 201105; d) M. Chen, R. Mishra, Y. Wu, K. Lee, H. Yang, *Adv. Opt. Mater.* **2018**, 6, 1800430.
- [11] L. R. Dalton, P. Gunter, M. Jazbinsek, O. P. Kwon, P. A. Sullivan, *Organic Electro-Optics and Photonics: Molecules, Polymers and Crystals*, Cambridge University Press, Cambridge, UK **2015**.
- [12] S. H. Lee, M. Jazbinsek, C. P. Hauri, O. P. Kwon, *CrystEngComm* **2016**, 18, 7180.
- [13] C. P. Hauri, C. Ruchert, C. Vicario, F. Ardana, *Appl. Phys. Lett.* **2011**, 99, 161116.
- [14] M. Shalaby, C. P. Hauri, *Nat. Commun.* **2015**, 6, 8439.
- [15] a) A. Schneider, M. Neis, M. Stillhart, B. Ruiz, R. U. A. Khan, P. Günter, *J. Opt. Soc. Am. B* **2006**, 23, 1822; b) M. Stillhart, A. Schneider, P. Günter, *J. Opt. Soc. Am. B* **2008**, 25, 1914.
- [16] C. Vicario, B. Monoszlai, M. Jazbinsek, S. H. Lee, O. P. Kwon, C. P. Hauri, *Sci. Rep.* **2015**, 5, 14394.
- [17] a) S. H. Lee, B. J. Kang, J. S. Kim, B. W. Yoo, J. H. Jeong, K. H. Lee, M. Jazbinsek, J. W. Kim, H. Yun, J. Kim, Y. S. Lee, F. Rotermund, O. P. Kwon, *Adv. Opt. Mater.* **2015**, 3, 756; b) S. J. Lee, B. J. Kang, M. H. Shin, S. C. Lee, S. H. Lee, M. Jazbinsek, H. Yun, D. Kim, F. Rotermund, O. P. Kwon, *Adv. Opt. Mater.* **2018**, 6, 1700930; c) M. H. Shin, S. H. Lee, B. J. Kang, M. Jazbinsek, W. Yoon, H. Yun, F. Rotermund, O. P. Kwon, *Adv. Funct. Mater.* **2018**, 28, 1805257.
- [18] a) A. Majkić, M. Zgonik, M. Jazbinsek, B. Ruiz, C. Medrano, P. Günter, *Appl. Phys. Lett.* **2014**, 105, 141115; b) C. M. Tu, L. H. Chou, Y. C. Chen, P. Huang, M. Rajaboopathi, C. W. Luo, K. H. Wu, V. Krishnakumar, T. Kobayashi, *Opt. Express* **2016**, 24, 5039; c) M. Tang, H. Minamide, Y. Wang, T. Notake, S. Ohno, H. Ito, *Opt. Express* **2011**, 19, 779.
- [19] J. Hebling, K. L. Yeh, M. C. Hoffmann, B. Bartal, K. A. Nelson, *J. Opt. Soc. Am. B* **2008**, 25, B6.
- [20] J. H. Jeong, B. J. Kang, J. S. Kim, M. Jazbinsek, S. H. Lee, S. C. Lee, I. H. Baek, H. Yun, J. Kim, Y. S. Lee, J. H. Lee, J. H. Kim, F. Rotermund, O. P. Kwon, *Sci. Rep.* **2013**, 3, 3200.
- [21] Z. Yang, L. Mutter, M. Stillhart, B. Ruiz, S. Aravazhi, M. Jazbinsek, A. Schneider, V. Gramlich, P. Günter, *Adv. Funct. Mater.* **2007**, 17, 2018.
- [22] B. J. Coe, J. A. Harris, I. Asselberghs, K. Wostyn, K. Clays, A. Persoons, B. S. Brunschwig, S. J. Coles, T. Gelbrich, M. E. Light, M. B. Hursthouse, K. Nakatani, *Adv. Funct. Mater.* **2003**, 13, 347.
- [23] a) G. A. Valdivia-Berroeta, E. W. Jackson, K. C. Kenney, A. X. Wayment, I. C. Tangen, C. B. Bahr, S. J. Smith, D. J. Michaelis, J. A. Johnson, *Adv. Funct. Mater.* **2020**, 30, 1904786; b) G. A. Valdivia-Berroeta, L. K. Heki, E. W. Jackson, I. C. Tangen, C. B. Bahr, S. J. Smith, D. J. Michaelis, J. A. Johnson, *Opt. Lett.* **2019**, 44, 4279; c) J. Shi, F. Liang, Y. He, X. Zhang, Z. Lin, D. Xu, Z. Hu, J. Yao, Y. Wu, *Chem. Commun.* **2019**, 55, 7950.
- [24] C. Bosshard, M. Bösch, I. Liakatas, M. Jäger, P. Günter, in *Nonlinear Optical Effects and Materials* (Ed.: P. Günter), Springer-Verlag, Berlin **2000**, Ch. 3.
- [25] a) O. Y.-H. Tai, C. H. Wang, H. Ma, A. K.-Y. Jen, *J. Chem. Phys.* **2004**, 121, 6086; b) M. Friebe, M. Meinke, *Appl. Opt.* **2006**, 45, 2838; c) B. D. Wilts, B. Wijnen, H. L. Leertouwer, U. Steiner, D. G. Stavenga, *Adv. Opt. Mater.* **2017**, 5, 1600879; d) M. Y. Livshits, J. J. Rack, *J. Phys. Chem. C* **2016**, 120, 26459; e) D. Aplitz, R. P. Bertram, N. Benter, W. Hieringer, J. W. Andreasen,

- M. M. Nielsen, P. M. Johansen, K. Buse, *Phys. Rev. E* **2005**, *72*, 036610.
- [26] a) F. D. J. Brunner, O. P. Kwon, S. J. Kwon, M. Jazbinsek, A. Schneider, P. Günter, *Opt. Express* **2008**, *16*, 16496; b) B. J. Kang, I. H. Baek, S. H. Lee, W. T. Kim, S. J. Lee, Y. U. Jeong, O. P. Kwon, F. Rotermund, *Opt. Express* **2016**, *24*, 11054.
- [27] J. H. Jeong, J. S. Kim, J. Campo, S. H. Lee, W. Y. Jeon, W. Wenseleers, M. Jazbinsek, H. Yun, O. P. Kwon, *Dyes Pigm.* **2015**, *113*, 8.
- [28] A. J. T. Lou, S. Righetto, C. Barger, C. Zuccaccia, E. Cariati, A. Macchioni, T. J. Marks, *J. Am. Chem. Soc.* **2018**, *140*, 8746.
- [29] a) J. Zyss, J. F. Nicoud, M. Coquillay, *J. Chem. Phys.* **1984**, *81*, 4160; b) P. Günter, C. Bosshard, K. Sutter, H. Arend, *Appl. Phys. Lett.* **1987**, *50*, 486; c) H. Hashimoto, Y. Okada, H. Fujimural, M. Morioka, O. Sugihara, N. Okamoto, R. Matsushima, *Jpn. J. Appl. Phys.* **1997**, *36*, 6754; d) G. Ferguson, C. Glidewell, J. N. Low, J. M. S. Skakle, J. L. Wardell, *Acta Crystallogr., Sect. C: Cryst. Struct. Commun.* **2001**, *57*, 315; e) A. Fkyerat, A. Guelzim, E. Baert, W. Paulus, G. Heger, J. Zyss, A. Périgaud, *Acta Crystallogr., Sect. B: Struct. Sci.* **1995**, *51*, 197; f) M. Y. Antipin, T. V. Timofeeva, R. D. Clark, V. N. Nesterov, F. M. Dolgushin, J. Wu, A. Leyderman, *J. Mater. Chem.* **2001**, *11*, 351; g) K. Piela, I. Turowska-Tyrk, M. Drozd, M. M. Szostak, *J. Mol. Struct.* **2011**, *991*, 42.
- [30] a) P. J. Kim, J. H. Jeong, M. Jazbinsek, S. B. Choi, I. H. Baek, J. T. Kim, F. Rotermund, H. Yun, Y. S. Lee, P. Günter, O. P. Kwon, *Adv. Funct. Mater.* **2012**, *22*, 200; b) S. H. Lee, B. J. Kang, B. W. Yoo, S. C. Lee, S. J. Lee, M. Jazbinsek, H. Yun, F. Rotermund, O. P. Kwon, *Adv. Funct. Mater.* **2017**, *27*, 1605583.
- [31] O. P. Kwon, S. J. Kwon, M. Jazbinsek, F. D. J. Brunner, J. I. Seo, C. Hunziker, A. Schneider, H. Yun, Y. S. Lee, P. Günter, *Adv. Funct. Mater.* **2008**, *18*, 3242.
- [32] F. Bureš, *RSC Adv.* **2014**, *4*, 58826.
- [33] J. Campo, F. Desmet, W. Wenseleers, E. Goovaerts, *Opt. Express* **2009**, *17*, 4587.
- [34] M. C. Flipse, R. de Jonge, R. H. Woudenberg, A. W. Marsman, C. A. van Walree, L. W. Jenneskens, *Chem. Phys. Lett.* **1995**, *245*, 297.
- [35] J. L. Oudar, D. S. Chemla, *J. Chem. Phys.* **1977**, *66*, 2664.
- [36] S. J. Kwon, O. P. Kwon, J. I. Seo, M. Jazbinsek, L. Mutter, V. Gramlich, Y. S. Lee, H. Yun, P. Günter, *J. Phys. Chem. C* **2008**, *112*, 7846.
- [37] a) S. R. Marder, J. W. Perry, W. P. Schaefer, *Science* **1989**, *245*, 626; b) P. J. Kim, J. H. Jeong, M. Jazbinsek, S. J. Kwon, H. Yun, J. T. Kim, Y. S. Lee, I. H. Baek, F. Rotermund, P. Günter, O. P. Kwon, *CrystEng-Comm* **2011**, *13*, 444.
- [38] J. Zyss, J. L. Oudar, *Phys. Rev. A* **1982**, *26*, 2028.
- [39] S. K. Kurtz, T. T. Perry, *J. Appl. Phys.* **1968**, *39*, 3798.
- [40] a) I. Ledoux, C. Lepers, A. Perigaud, J. Badan, J. Zyss, *Opt. Commun.* **1990**, *80*, 149; b) C. Bosshard, K. Sutter, P. Günter, *J. Opt. Soc. Am. B* **1989**, *6*, 721.
- [41] S. van Bezouw, J. Campo, S.-H. Lee, O.-P. Kwon, W. Wenseleers, *J. Phys. Chem. C* **2015**, *119*, 21658.
- [42] F. D. J. Brunner, S. H. Lee, O. P. Kwon, T. Feurer, *Opt. Mater. Express* **2014**, *4*, 1586.
- [43] a) K. M. Hugar, H. A. t. Kostalik, G. W. Coates, *J. Am. Chem. Soc.* **2015**, *137*, 8730; b) J. Fan, A. G. Wright, B. Britton, T. Weissbach, T. J. G. Skalski, J. Ward, T. J. Peckham, S. Holdcroft, *ACS Macro Lett.* **2017**, *6*, 1089.
- [44] T. Seidler, K. Stadnicka, B. Champagne, *Adv. Opt. Mater.* **2014**, *2*, 1000.
- [45] G. M. Sheldrick, *Acta Crystallogr., Sect. A: Found. Crystallogr.* **2008**, *64*, 112.
- [46] K. Kuroyanagi, M. Fujiwara, H. Hashimoto, H. Takahashi, S. I. Aoshima, Y. Tsuchiya, *Jpn. J. Appl. Phys.* **2006**, *45*, 4068.
- [47] F. D. J. Brunner, A. Schneider, P. Günter, *Appl. Phys. Lett.* **2009**, *94*, 061119.
- [48] M. Fujiwara, M. Maruyama, M. Sugisaki, H. Takahashi, S. I. Aoshima, R. J. Cogdell, H. Hashimoto, *Jpn. J. Appl. Phys.* **2007**, *46*, 1528.